lubricants

MDPI

Article

Structure Modulation and Self-Lubricating Properties of Porous TiN–MoS_2 Composite Coating Under Humidity–Fluctuating Conditions

Tiancheng Ye [1,2], Kai Le [3,4], Ganggang Wang [2], Zhenghao Ren [2], Yuzhen Liu [3], Liwei Zheng [2,*], Hui Tian [1,*] and Shusheng Xu [3,4]

[1] College of Chemistry and Chemical Engineering, Yantai University, Yantai 264005, China
[2] Shandong Laboratory of Advanced Materials and Green Manufacturing at Yantai, Yantai 264000, China
[3] State Key Laboratory of Solid Lubrication, Lanzhou Institute of Chemical Physics, Chinese Academy of Sciences, Lanzhou 730000, China; ssxu@licp.cas.cn (S.X.)
[4] Yantai Zhongke Research Institute of Advanced Materials and Green Chemical Engineering, Yantai 264000, China
* Correspondence: liweizheng@amgm.ac.cn (L.Z.); tianhui@ytu.edu.cn (H.T.)

Abstract: To improve the friction performance and service life of protective coatings in humidity-fluctuating environments, porous hard titanium nitride (TiN)–molybdenum disulfide (MoS_2) composite coatings were prepared by using direct current magnetron sputtering (DCMS) with the mode of oblique angle deposition (OAD) and chemical vapor deposition (CVD) technologies. The structure and chemical component were characterized by field emission scanning electron microscopy (FESEM), energy dispersive spectrometer (EDS), grazing incidence X-ray diffraction (GIXRD), atomic force microscopy (AFM), X-ray photoelectron spectroscopy (XPS), and Raman spectroscopy. The tribological properties of these TiN–MoS_2 composite coatings were investigated. The results indicate that the porous TiN–MoS_2 composite coating exhibited outstanding friction performance and long service life under humidity-fluctuating environments. At the initial 20% relative humidity (RH) stage, the MoS_2 on the porous TiN–MoS_2 composite coating surface worked as an effective lubricant; thus, the coating demonstrated excellent lubrication performance, and the friction coefficient (COF) was about 0.05. As the humidity was alternated to 70% RH, the lubrication effect diminished due to the production of molybdenum oxide (MoO_3), and the COF was about 0.2, which was attributed to the degradation of MoS_2 on the wear track and the release of fresh MoS_2 from the porous TiN matrix. After the environmental conditions shifted from 70% to 20% RH, the MoO_3 was removed, and the lubrication effect was restored. In summary, TiN–MoS_2 porous composite coating offers a promising approach for lubrication in humidity-fluctuating environments.

Keywords: oblique angle deposition; low surface roughness; porous structure; TiN–MoS_2 composite coating; humidity-fluctuating environments

Received: 20 December 2024
Revised: 25 January 2025
Accepted: 27 January 2025
Published: 1 February 2025

Citation: Ye, T.; Le, K.; Wang, G.; Ren, Z.; Liu, Y.; Zheng, L.; Tian, H.; Xu, S. Structure Modulation and Self-Lubricating Properties of Porous TiN–MoS_2 Composite Coating Under Humidity–Fluctuating Conditions. *Lubricants* **2025**, *13*, 61. https://doi.org/10.3390/lubricants13020061

1. Introduction

In the aerospace field, a molybdenum disulfide (MoS_2) coating is widely used as a lubricant in precise bearings because of its excellent friction properties in vacuum and dry-air environments [1,2]. The low shear strength of MoS_2 originates from the weak interatomic interactions between its layered structure, resulting in very low friction [3–5]. However, in practical applications, the precision moving components of spacecraft are often exposed to humid environments for a while during operation (especially in coastal cities) [6] or

encounter humidity fluctuations during the flight cycle [7]. In general, MoS_2 easily adsorbs water molecules and oxygen in wet-air environments, leading to oxidation and deterioration of the tribological properties. In addition, the low hardness, weak adhesion, and poor wear resistance of MoS_2 also limit its wide application [8–11]. Compared with MoS_2, a titanium nitride (TiN) coating has the characteristics of chemical stability, wear resistance, and high hardness. Thus, it is always widely used in many fields, such as high-speed steel-cutting tools and punches and metal-forming parts [12–14]. In practical applications, a protective coating for precision moving components has to possess the excellent low friction characteristics of a solid lubricant, high wear resistance, and the high bearing capacity of hard ceramic materials. Therefore, it is crucial to design and fabricate an anti-wear coating that can slowly release the solid lubricant phase in order to maintain low friction in high or humidity-fluctuating environments.

In previous reports, MoS_2 was incorporated into the metal, oxide, or TiN matrix to form a composite material [15–19]. Yuhang Yao et al. [15] prepared a Ni–MoS_2 composite coating on an LST-treated SS substrate using the ECD process. The application of microgrooves changed the growth pattern of the coating, reduced the wear of the coating, and was able to store and collect MoS_2 flakes to produce secondary lubrication. Yijing Wang et al. [16] prepared Al_2O_3 coating and Al_2O_3/Ag composite coating using the APS technology and synthesized MoS_2 in situ at the coating defects using the hydrothermal method to obtain Al_2O_3/MoS_2 composite coating and Al_2O_3/Ag/MoS_2 composite coating. The composite coating surface is denser and has better mechanical properties and lubrication properties. Gangopadhyay et al. [17] investigated the effect of substrate bias voltage on the structure and mechanical properties of TiN–MoS_2 composite coatings fabricated by a pulsed direct-current closed-field unbalanced magnetron sputtering (CFUBMS) technology. The results showed that the composite coating became dense under a certain substrate bias voltage, which improved the mechanical properties and wear resistance of TiN–MoS_2 composite coatings. Gilmore et al. [19] altered the position of the substrate and target material to adjust the coating composition, and the prepared TiN–MoS_2 composite coating presented high hardness and low friction. Although these approaches can improve the mechanical and tribological properties of coatings, they still have certain limitations. The sputtering deposition rates of TiN and MoS_2 are different during the fabrication process due to the different sputtering yields of their phases, resulting in a lack of order in the structure of the coating. Additionally, there are no channels for releasing lubricants outside from the interior of the TiN–MoS_2 composite coating to achieve robust lubrication performance in high or humidity-fluctuating environments.

To prepare an ordered and controllable coating structure, laser texturing technology [20] and reactive ion etching [21] techniques were employed to texture the coating surface with regular reservoirs, which could be filled with solid lubricants. The size reservoirs at the micron scale were too large to achieve robust lubrication performance for the precision moving component due to the limitation of the fabrication techniques. Notably, the oblique angle deposition (OAD) [22] technique is a promising, attractive physical vapor deposition (PVD) pathway for producing nanostructured and sculpted thin films with open porosity, controlled texture, and anisotropic characteristics [23–25]. Our group [22] reported a TiCN coating with lots of small surface reservoirs that was prepared by combining multi-arc ion plating with OAD technology. Solid lubricants were then filled into these reservoirs to prepare a TiCN–MoS_2 composite coating, which exhibited a low friction coefficient in an environment with variable humidity. However, the surface particles of the TiCN coatings were relatively large, which limited their use in certain precision instruments. In comparison, the coating without large surface particles prepared by magnetron sputtering was relatively smooth [26,27]. Ren et al. [26] reported that a TiCN

coating prepared by combining multi-arc ion plating and magnetron sputtering techniques exhibited smooth morphologies and better corrosion resistance. Zhang et al. [27] found that a TiN–WC coating prepared on the TiN interlayer using magnetron sputtering technology exhibited smooth surface particles and improved tribological performance. However, the porous structure of the nitride ceramic coating was not easy to modulate via the sputtering technique.

Herein, porous TiN coatings with different modulated microstructures were prepared by combining direct current magnetron sputtering (DCMS) and OAD technologies. The effect of OAD on porosity and pore size was investigated at various target currents. The structural variation of the coatings was investigated by using field emission scanning electron microscope (FESEM), grazing incidence X-ray diffraction (GIXRD), and atomic force microscopy (AFM). Nanoindentation tests were carried out to evaluate the effect of OAD on the mechanical properties of the coatings. Finally, MoS_2 was filled into the pores by chemical vapor deposition (CVD), and the tribological properties were investigated in various humidity as well as humidity-fluctuating environments. The result indicated that porous TiN–MoS_2 composite coating exhibited excellent friction performance. Energy-dispersive X-ray spectroscopy (EDS), X-ray photoelectron spectroscopy (XPS), and Raman measurement of the wear tracks further revealed its self-lubricating mechanism in these environments.

2. Experimental Details

2.1. Sample Preparation

DCMS technology was used to prepare TiN coatings on 304 stainless steel slices (20 mm × 20 mm × 5 mm) and silicon wafers at various target currents and deposition angles. The 304 steel slices with abrasive SiC papers from 400 to 2000 grit, followed by mirror polishing with a diamond suspension. To ensure uniform coating, the surface roughness parameter Ra of the surface must be less than 50 nm. The 304 stainless steel slices and silicon wafers were first ultrasonically treated with acetone for 15 min, followed by ethanol for 5 min. Before coating deposition, the substrate was bombarded with argon ions in a vacuum chamber to remove surface contaminants. Subsequently, a titanium intermediate layer was deposited on the substrate to increase the coating–substrate adhesion [28,29]. The final step involved depositing the TiN coatings. During the deposition procedure, the deposition angle (the angle between the substrate normal and the target normal) was set as 0° and 80°, respectively. TiN coatings with deposition angles of 0° and 80° were referred to as TiN (0°) and TiN (80°) coatings, respectively. Moreover, to modulate the pore size and density, the TiN (80°) coating was further deposited at various target currents. The detailed parameters for the specific deposition of TiN coatings are summarized in Table 1.

Table 1. Preparation parameter of TiN coatings.

Item	Parameter
Target to substrate distance	14 cm
Bias voltage	0 V
Gas ratio (N_2/N_2 + Ar)	1:3
Base pressure	8×10^{-3} Pa
Deposition time	120 min
Temperature	30 °C
Current	6 A,8 A,10 A
Pressure	0.3 Pa

MoS_2 was added into the TiN (0°) and TiN (80°) coatings by the CVD method. $(NH_4)_2MoS_4$, the precursor of MoS_2, was purchased from Aladdin Biotech (CAS 15060-55-6). It was dissolved in deionized water and sonicated to guarantee full dissolution, yielding an aqueous solution with a 20 mg/mL concentration. The as-prepared TiN coatings were completely immersed in the $(NH_4)_2MoS_4$ solution and ultrasonically treated for 3 h to ensure that the solution permeated all the pores of the coatings. Subsequently, the samples were dried and placed in a tube furnace with a based vacuum of 10 Pa. A mixed gas of H_2 with a flow rate of 40 sccm and N_2 with a flow rate of 80 sccm was introduced as the reaction gas, and the pressure was 100 kPa during the reaction process. The tube furnace temperature was gradually increased to 400 °C at a rate of 10 °C/min and maintained for 60 min. After treatment, the $(NH_4)_2MoS_4$ in the coating pores could react to generate MoS_2, and, thus, a TiN–MoS_2 composite coating was completely fabricated.

2.2. Coating Structure Characterization

The surface and cross-sectional morphologies of the TiN coatings were observed by using a field emission scanning electron microscope (FESEM, JSM-7610F, JEOL Ltd., Tokyo, Japan). The element distribution on the cross-section and wear scar of the TiN–MoS_2 composite coating was observed by using energy-dispersive X-ray spectroscopy (EDS, NORAN System 7, Thermo Fisher Scientific, Waltham, MA, USA). FESEM images were analyzed by the open-source ImageJ software (v1.8.0) to evaluate the surface pore size and porosity of the coating. For ImageJ analysis, the FESEM images were converted to 8-bit mode. Brightness and contrast (B&C) adjustment was used to remove the noise in the background of the images. Automatic thresholding was then used to convert images to binary (black and white), in which the black areas represent the pores, and the white areas represent the coating surface. Atomic force microscopy (AFM, Dimension 3100, Veeco Instruments Inc., Plainview, NY, USA) was used to observe the surface roughness of the coatings. The scan range of the coating was an area of 50 × 50 μm^2. The images obtained at a resolution of 256 × 256 pixels were processed by the Gwyddion software. The crystal structure of the coating was characterized by grazing incidence X-ray diffraction (GIXRD, D8, Bruker, Mannheim, Germany) using Cu-Kα radiation, a scanning rate of 10°/min, and a scanning range of from 5° to 90°. The nanohardness (H) and Young's modulus (E) of the deposited coatings were measured by using a nanoindenter (UNHT, Anton Paar, Graz, Austria) with a diamond Berkovich diamond tip with a radius of 20 nm. The indentation depth was kept at approximately 10% of the coating thickness to ensure that the substrate hardness did not affect the coating. All TiN coatings specimens were subjected to a maximum load of 1 mN with a dwell time of 0 s at the maximum load, and the loading and unloading rates were 1 mN/min, respectively. Five indentation measurements were performed for each coating sample to calculate the average value. The elastic modulus was calculated by using the following equation:

$$\frac{1}{E_r} = \frac{1-\nu^2}{E} + \frac{1-\nu_i^2}{E_i}$$

where E and v represent the substrate's modulus of elasticity and Poisson ratio, and E_i and V_i are the indenter's parameters, respectively. The Poisson ratio of the TiN coating is about 0.23.

The elemental valence states and phase structures of the wear tracks were analyzed by using X-ray photoelectron spectroscopy (XPS, Thermo escalab 250Xi, Thermo Fisher, MA, USA) with monochromatic Al Kα (hv = 1486.6 eV) radiation. To obtain high-resolution spectra, the electron energy analyzer was operated at a pass energy of 50 eV. The step size of 0.05 eV was employed and each peak was scanned five times. The binding energy

(BE) scale was calibrated using the C 1 s peak of graphite at BE = 284.8 eV. The Sherry method was used to subtract the background, and the Gaussian–Lorentz fitting method was used for peak fitting. Raman spectroscopy (DXR2, Thermo Fisher Scientific, Waltham, MA, USA) with a laser wavelength of 532 nm was used for surface mapping to measure the distribution of MoS_2 on the composite coating surface and wear tracks.

2.3. Friction Properties

The tribological properties of the composite coatings were investigated with a ball-on-disk rotating friction tester at room temperature and various humid conditions. The friction tests were conducted with a constant load of 2 N, a rotation speed of 200 rpm, and a rotation radius of 4 mm. The counterpart is an 8 mm diameter Si_3N_4 ball with a maximum Hertzian contact pressure of 0.35 GPa. The friction tests were carried out in air at 20 and 70% RH, respectively, with the corresponding test times of 3000 s. In the variable humid friction test, the humidity was changed between 20 and 70% RH. Each humidity stage lasted for 300 s, and the total sliding cycle time was 2700 s. Wear rates were determined using a three-dimensional white light microscope (LSCM, DCM8, Leica, Germany), which measured the three-dimensional topography.

3. Results and Discussion

3.1. Structural Analysis

The surface and cross-sectional morphology of the TiN (0°) and TiN (80°) coatings are shown in Figure 1. The surface morphology of the TiN (0°) coating presents a dense structure, as shown in Figure 1a. In comparison, the surface morphology of the TiN (80°) coating has a loose structure (Figure 1b). The loose structure is a characteristic of OAD coatings, and the pores are created by the shielding effect during the coating growth process [30,31]. In addition, the cross-sectional morphology of the TiN (0°) coating reveals a vertical columnar structure. The columns are tightly bonded together to thus form a dense structure (Figure 1c). Compared with the TiN (0°) coating, the TiN (80°) coating presents an inclined nanocolumn structure. The columnar structures are separated from each other to thus form a loose structure, as illustrated in Figure 1d, resulting from the shadowing effect of plasma deposition during film formation [32]. Additionally, the thickness of the TiN (0°) coating is 1.852 μm, while the thickness of the TiN (80°) coating is 1.131 μm after the same deposition time. This was because the incident particle flux received by the substrate decreased as the deposition angle increased [33]. Thus, the TiN (80°) coating is thinner than the TiN (0°) coating.

To modulate the pore size of the TiN (80°) coatings, the deposition processes were applied at different target currents of 6, 8, and 10 A, which were labeled as TiN (80°) 6A, TiN (80°) 8A, and TiN (80°) 10A, respectively. The same deposition processes were also conducted for the TiN (0°) coatings deposition for comparison, which were labeled as TiN (0°) 6A, TiN (0°) 8A, and TiN (0°) 10A, respectively. As shown in Figure 2a–c, the TiN (0°) 6A and TiN (0°) 8A coatings possess a dense and smooth surface, but a coarser texture appears in TiN (0°) 10A. This can be attributed to an increase in the deposition species and ion bombardment [31]. The TiN (80°) 6A coating exhibits a dense surface structure (Figure 2d). In contrast, the TiN (0°) 8A and TiN (0°) 10A coatings reveal a pretty loose and porous structure (Figure 2e,f). To further investigate the porosity and pore size of the TiN (80°) coatings, the ImageJ program was used to semi-quantitatively assess the looseness and to differentiate between the columnar structure and the pores. The results are given in Figure 3. It can be seen that the porosity and pore size of the TiN (80°) 8A are 13.02% and 110 nm, respectively. As the target current increased from 8 to 10 A, the porosity reduced marginally while the pore size increased to 123 nm. As the target current increases, the

atomic ionization rate can also strengthen, leading to a rise in the number of argon ions sputtering the target. The heightened bombardment results in an increase in the amount of the ejected atoms of the target. These atoms can more freely reach the surface of the substrate, promoting coating growth and formation of the column gaps [31]. Therefore, the size of these column gaps can expand when the target current, as well as the number of ejected atoms, increases.

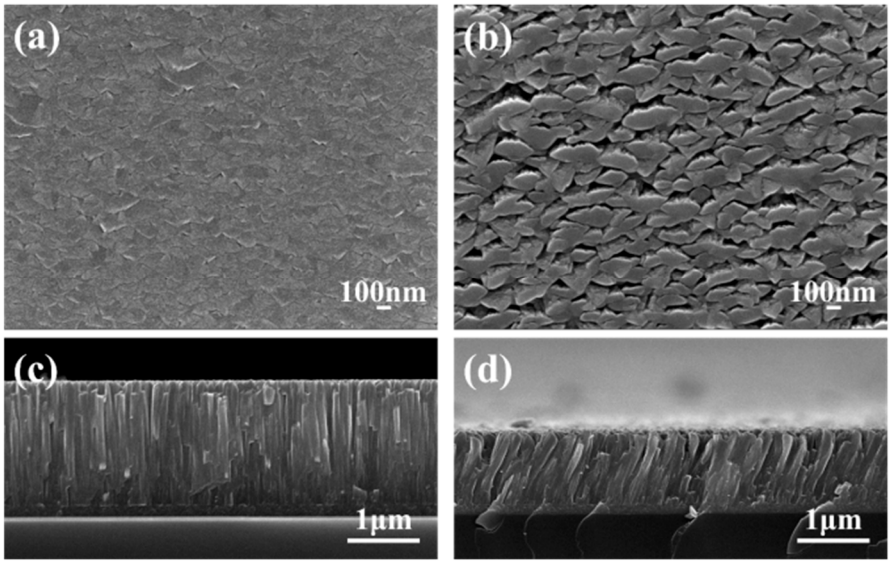

Figure 1. Surface and cross-sectional FESEM images of (**a**,**c**) TiN (0°) coating and (**b**,**d**) TiN (80°) coating.

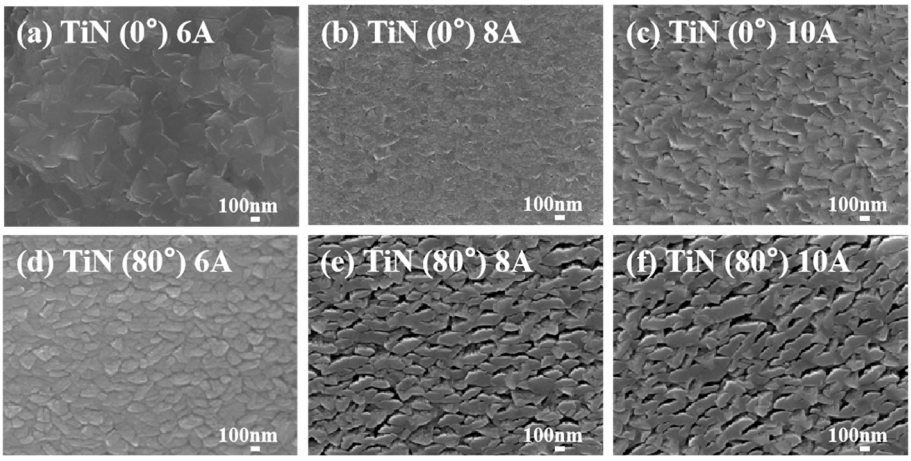

Figure 2. FESEM images of top views of (**a**–**c**) TiN (0°) coatings and (**d**–**f**) TiN (80°) coatings deposited under different target currents.

AFM was employed to analyze the surface morphology of the nano-columnar TiN coatings on the silicon substrate, as shown in Figure 4. The roughness of the TiN coating increased with the target current increase, and the TiN (80°) coatings were rougher than the TiN (0°) coatings. The TiN (80°) coatings had a ridge-like featured surface, which made the surface fluctuate greatly and resulted in high roughness. As previously reported [24], the surface roughness of the coating prepared by OAD was higher than those deposited by conventional methods due to the self-shadowing effect during the coating growth process. Furthermore, the increased roughness indicates that the coatings made by OAD have a larger surface disorder and porosity.

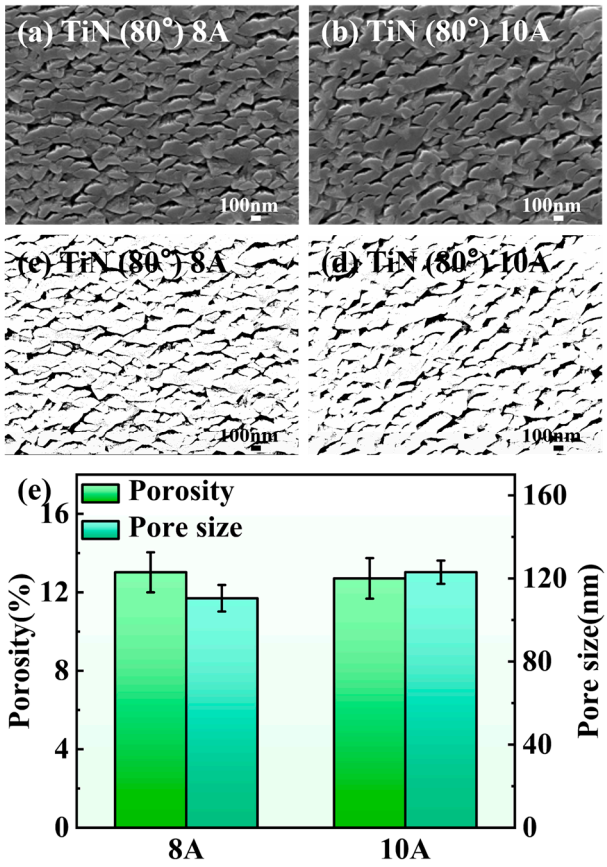

Figure 3. FESEM images of top views of (**a**) TiN(80°) 8 A and (**b**) TiN(80°) 10 A; binary black and white images (**c**,**d**) in ImageJ corresponding to (**a**,**b**); (**e**) porosity and pore size of TiN (80°) coatings corresponding to (**a**,**b**).

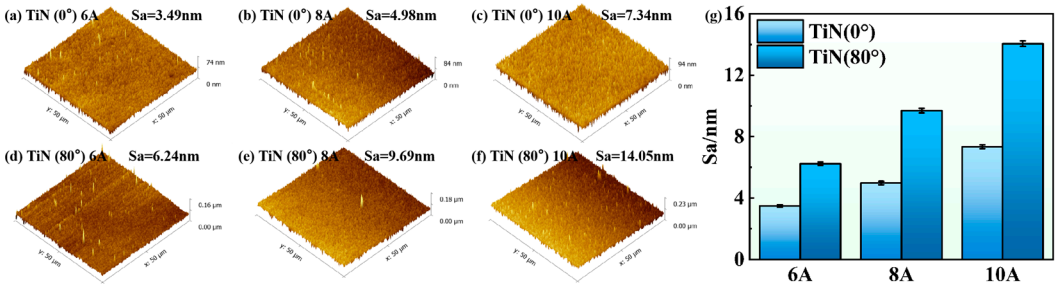

Figure 4. Surface characterization of (**a**–**c**) TiN (0°) and (**d**–**f**) TiN (80°) coating by AFM topography (with average roughness parameters shown in (**g**)).

Figure 5 displays the GIXRD patterns of TiN (0°), TiN (80°), TiN (0°)–MoS_2, and TiN (80°)–MoS_2 composite coating. It could be observed that both the TiN (80°) and TiN (0°) coatings show a predominantly face-centered cubic structure and prominent (220) texture. The main diffraction peaks of the TiN coatings at 36.82°, 42.77°, 62.08°, 74.41°, and 78.33° correspond to the (111), (200), (220), (311), and (222) planes, respectively, indicating the formation of polycrystalline TiN coatings [34,35]. Compared with the TiN coatings, the TiN (80°)–MoS_2 and TiN (0°)–MoS_2 composite coatings display a diffraction peak at a 2θ angle of 14.37°, corresponding to the (002) plane of MoS_2. Furthermore, the (002) plane of MoS_2, which is aligned parallel to the substrate surface, can contribute to excellent tribological properties and enhance oxidation resistance in humid environments [36,37].

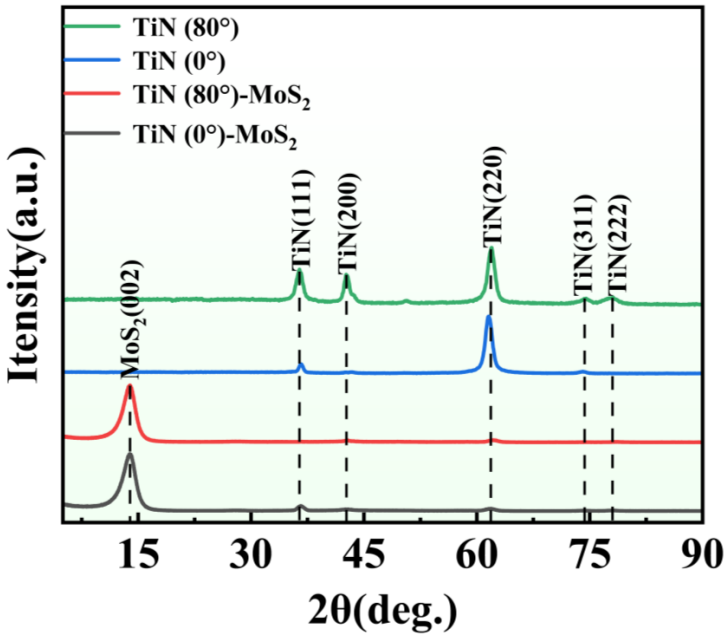

Figure 5. GIXRD patterns of TiN (0°), TiN (80°), TiN (0°)–MoS_2, and TiN (80°)–MoS_2 composite coating.

Figure 6 presents the EDS results of the cross-sectional TiN (0°)–MoS_2 and TiN (80°)–MoS_2 composite coatings. It can be found that the TiN (0°)–MoS_2 composite coating has a few molybdenum (Mo) and sulfur (S) elements. However, the TiN (80°)–MoS_2 composite coating has a great amount of Mo and S elements. This is because the TiN (0°) coating has a compact structure that prevents infiltration of the $(NH_4)_2MoS_4$ solution during ultrasonic treatment. In contrast, the TiN (80°) coating possesses an open and porous structure. Consequently, due to diffusion during ultrasonic treatment, a large quantity of $(NH_4)_2MoS_4$ solution becomes trapped in the pores of the TiN (80°) coating, which could be subsequently converted into MoS_2 after high-temperature heat treatment.

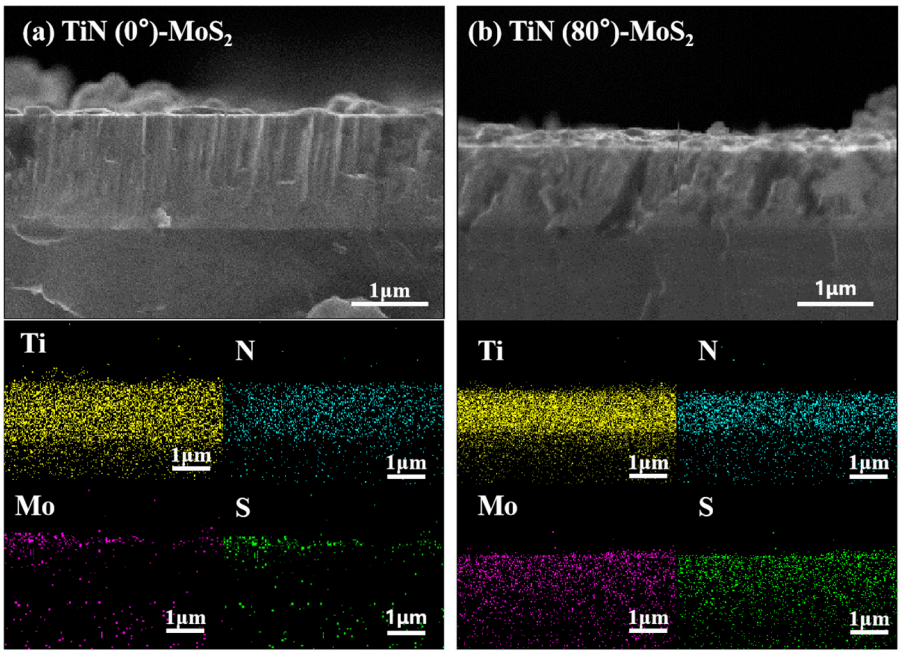

Figure 6. EDS analysis of cross-sectional of (**a**) TiN (0°)–MoS_2 and (**b**) TiN (80°)–MoS_2 composite coating deposited at 8 A.

3.2. Mechanical and Tribological Properties

The hardness (H) and elastic modulus (E) variation of the TiN coatings are presented in Figure 7. Under a load of 1 mN, the hardness of the TiN (0°) and TiN (80°) coatings is approximately 8.3 ± 0.3 and 6.2 ± 0.6 GPa, respectively. The elastic modulus (E) for these coatings is approximately 216.8 ± 19.7 and 183.1 ± 24.6 GPa, respectively. The mechanical properties of the TiN (80°) coating degraded due to the separation of TiN columnar structure, whereas the high porosity reduced the dense coating's load-carrying capacity. Overall, the TiN (0°) and TiN (80°) coatings have comparable mechanical properties. Furthermore, the hardness of the porous coating exceeds that of the 304 steel substrate (3.4 GPa) [38], indicating that the coating can also provide a modest enhancement in the load-bearing capacity.

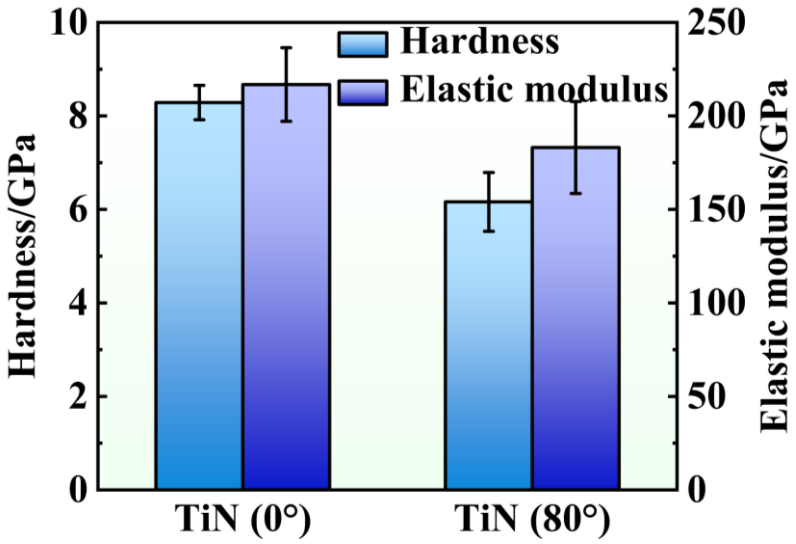

Figure 7. Hardness and elastic modulus of TiN (0°) and TiN (80°) coatings.

To investigate the tribological behavior of the TiN-based coatings with the filled lubricant MoS_2, ball-on-disc friction tests were performed at 20 and 70% RH. As shown in Figure 8a, the COF of the TiN (0°)–MoS_2 composite coating is about 0.05 for 1500 s before gradually increasing to about 0.1 at 20% RH. At 70% RH, the COF of the TiN (0°)–MoS_2 composite coating gradually increases to about 0.7 with the increase in the times. However, at 20% RH, the COF of the TiN (80°)–MoS_2 composite coating remains stable at 0.05 with minimal fluctuation. At 70% RH, the COF of the TiN (80°)–MoS_2 composite coating is about 0.3 for 2400 s before gradually increasing, as shown in Figure 8b. This finding indicates that the TiN (80°)–MoS_2 composite coating has an extended service life. The difference in lubrication performance of the TiN –MoS_2 composite coatings at 20% RH and 70% RH can be attributed to the distribution of the MoS_2 lubricant. The TiN (0°) coating features a dense structure that leads to the MoS_2 lubricant accumulating on the surface rather than penetrating the interior of the coating. During the friction process, the MoS_2 lubricant on the surface may continuously degrade or detach, increasing the friction coefficient over time. In contrast, the MoS_2 lubricant was filled into the pores of the TiN (80°) coating. As a result, the MoS_2 lubricant can be released from these pores, helping to maintain a stable friction coefficient during the friction process. Figure 8c,d shows the friction coefficients of the TiN (0°)–MoS_2 and TiN (80°)–MoS_2 composite coatings in humidity-fluctuating environments. The friction test consists of an initial 20% RH stage, followed by an elevation to a 70% RH stage, and, finally, a return to a 20% RH stage, of which each stage is sustained for 300 s. In the initial stage of the friction test at 20% RH, both the COFs of the TiN

(0°)–MoS_2 and TiN (80°)–MoS_2 composite coatings quickly decrease to approximately 0.05 following a brief running-in period. When the ambient humidity is transformed to 70% RH, the COF of the TiN (0°)–MoS_2 composite coating gradually increases, while the COF of the TiN (80°)–MoS_2 composite coating stabilizes at approximately 0.2. When the ambient humidity returns to 20% RH, the COF of the TiN (0°)–MoS_2 composite coating initially decreases after a brief running-in period before steadily increasing. In contrast, the COF of the TiN (80°)–MoS_2 composite coating stabilizes at 0.05 following a short running-in period. It is noteworthy to notice that, during the subsequent stage of humidity fluctuation, the COF of the TiN (0°)–MoS_2 composite coating gradually increases, whereas the COF of the TiN (80°)–MoS_2 composite coating is almost reversible under humidity fluctuation. In the initial stage of 20% RH, the low COF was primarily influenced by the shear strength of the MoS_2 that remained on the coating surface or was released from the internal pores, as they were not entirely removed from the coating surface during the friction process. At 70% RH, MoS_2 reacts with H_2O and O_2 to produce MoO_3, which diminishes the lubrication effect. Therefore, the COF of the TiN (0°)–MoS_2 composite coating gradually increases, while the TiN (80°)–MoS_2 composite coating maintains its lubrication performance, and the COF is about 0.2. This is because MoS_2 is continuously released from the interior of the porous TiN (80°) matrix.

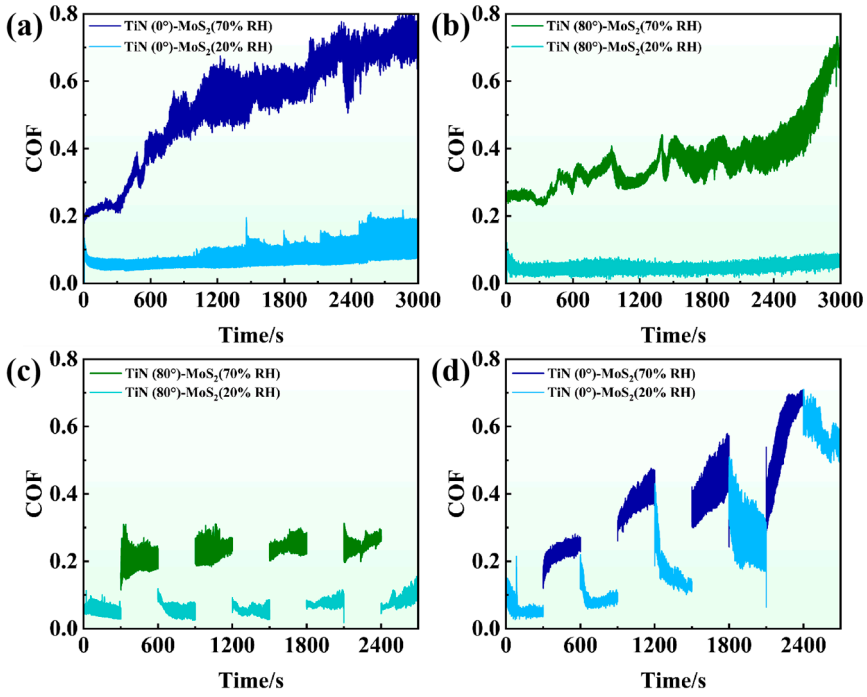

Figure 8. COF curves of (**a**) TiN (0°)–MoS_2 and (**b**) TiN (80°)–MoS_2 composite coatings in stable environment of 20 and 70% RH; COF curves of (**c**) TiN (0°)–MoS_2 and (**d**) TiN (80°)–MoS_2 composite coatings in the humidity-fluctuating environment between 20 and 70% RH.

Analyses of the worn surface and the wear rate of TiN–MoS_2 composite coatings are shown in Figure 9a–f. For the TiN (80°)–MoS_2 composite coatings, the wear tracks are very shallow, indicating the excellent wear resistance of the TiN (80°)–MoS_2 composite coating. In contrast, the wear tracks of the TiN (0°)–MoS_2 composite coatings are deeper than those of the TiN (80°)–MoS_2 coatings. Wear grooves along the sliding direction could be clearly seen. The MoS_2 lubricant in the pores of the TiN (80°)–MoS_2 composite coatings is released during the sliding process and plays a lubricating and wear-reducing role. In addition, it can be clearly observed that there is debris accumulation on both sides of the wear tracks. Figure 9g summarizes the wear rate of the TiN (0°)–MoS_2 and TiN (80°)–MoS_2

composite coatings at different times. The wear rates of both coatings increase over time. However, the TiN (80°)–MoS_2 composite coatings exhibit a lower wear rate than that of the TiN (0°)–MoS_2 composite coatings at the same time, indicating superior wear resistance.

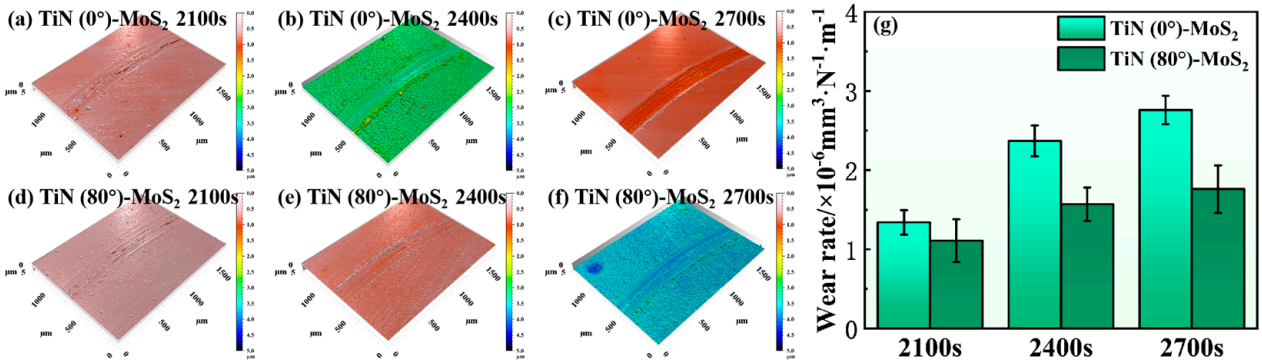

Figure 9. Worn surface of TiN–MoS_2 composite coatings: (**a**–**c**) 3D profilometer image of TiN (0°)–MoS_2 composite coatings at 2100 s, 2400 s, and 2700 s, respectively; (**d**–**f**) 3D profilometer image of TiN (80°)–MoS_2 composite coatings at 2100 s, 2400 s, and 2700 s, respectively; (**g**) wear rate of TiN–MoS_2 composite coatings over time.

To elucidate the wear mechanisms of the TiN (0°)–MoS_2 and TiN (80°)–MoS_2 composite coatings in a humidity-fluctuating environment, the surface morphology and elemental distribution of the wear tracks were observed. Figures 10 and 11 show the FESEM and corresponding EDS images of the wear tracks during the final three stages of the friction test in humidity-fluctuating environments (i.e., 20% RH for 2100 s, 70% RH for 2400 s, and 20% RH for 2700 s). As shown in Figure 10a–c, it can be seen that there is wear debris powder distributed around the wear tracks, and the elements Mo and S are more concentrated at the edge of the wear tracks. A similar phenomenon has also been observed in Figure 11a–c. This finding indicates that MoS_2 served as a lubricant during the friction process and was subsequently transferred to the edge of the wear tracks. It can also be found that the signals of the elements Mo and S on the wear track of the TiN (0°)–MoS_2 composite coating gradually diminish as friction progresses, while the signals from the elements Mo and S on the wear track of the TiN (80°)–MoS_2 composite coating remain detectable. In addition, compared to 70% RH, the Mo and S signals on the wear track of the TiN (80°)–MoS_2 composite coating are more pronounced at 20% RH. These results indicate that, during the friction test with fluctuating ambient humidity, the MoS_2 lubricant can be released from the pores of the TiN (80°)–MoS_2 composite coating and aggregate at the friction-sliding interface to play a lubricating role. Due to its dense structure, the TiN (0°)–MoS_2 composite coating hardly stores the MoS_2 lubricant at all. During friction testing, the MoS_2 lubricant on the surface degraded and was removed, leading to lower lubrication performance than that of the TiN (80°)–MoS_2 composite coating. Additionally, the oxygen signal on the wear track of the TiN–MoS2 composite coatings is faint at 20% RH but becomes more pronounced at 70% RH, which can be attributed to the reaction among the MoS_2, H_2O, and O_2 during friction at 70% RH. Subsequently, during the friction process at 20% RH, the oxide product was mechanically removed.

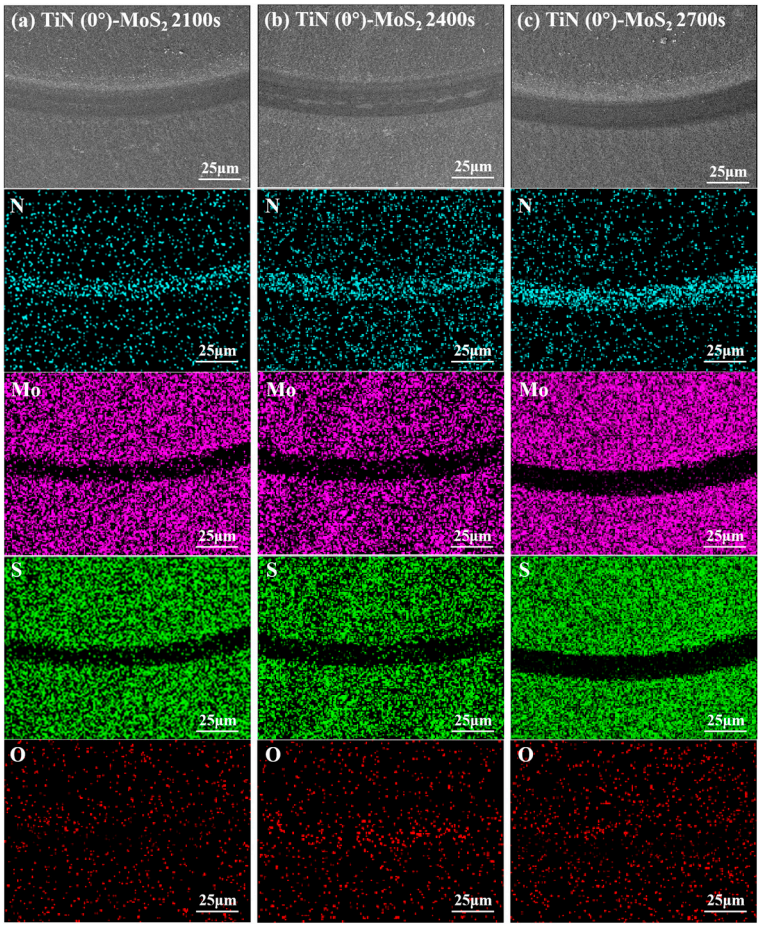

Figure 10. FESEM images and EDS mapping of the wear tracks of TiN–MoS_2 composite coatings during the humidity transition friction test: (**a**) TiN (0°)–MoS_2, 20% RH, 2100 s; (**b**) TiN (0°)–MoS_2, 70% RH, 2400 s; (**c**) TiN (0°)–MoS_2, 20% RH, 2700 s.

Figure 12 shows the XPS spectra of the wear tracks from the TiN (0°)–MoS_2 and TiN (80°)–MoS_2 composite coatings that were acquired in the 70% RH condition. It can be seen that both the TiN (0°)–MoS_2 and TiN (80°)–MoS_2 composite coatings have a peak at a binding energy of 226.28 eV corresponding to the S 2 s peak of MoS_2 [39], two peaks at 229.01 eV and 232.18 eV correspond to the Mo $3d_{5/2}$ and Mo $3d_{3/2}$ of MoS_{2-x}, and two peaks at 233.08 eV and 230.09 eV correspond to the Mo $3d_{5/2}$ and Mo $3d_{3/2}$ of MoS_2 (Mo^{4+}), respectively. In addition, the peak in binding energy at 235.67 eV corresponds to the Mo^{6+} (Mo-O bond) in MoO_3 [40,41], meaning that the MoS_2 is oxidized to generate the MoO_3 under a highly humid environment.

It is noteworthy that the formation of MoO_3 can significantly reduce friction. However, the COF of the TiN (80°)–MoS_2 composite coating remains low and stable under humidity fluctuations. Raman spectroscopy was used to analyze the distribution of MoS_2 and MoO_3, further investigating the lubrication mechanism of the composite coating (Figure 13). The A_{1g} and the $E^1{}_{2g}$ peaks of MoS_2 are attributed to the out-of-plane vibration of molybdenum and sulfur atoms and the in-plane vibration of sulfur atoms, respectively [42,43]. It can be seen that MoS_2 signals on the wear tracks of the TiN (0°)–MoS_2 composite coating gradually weaken (Figure 13a–c). However, the peak intensity of the MoS_2 signals on the TiN (80°)–MoS_2 wear track at 20% RH is higher than that at 70% RH (Figure 13d–f). In addition, the MoO_3 signal intensity on the wear scars of all the TiN–MoS_2 composite coatings is weak at 20% RH but stronger at 70% RH. This result is consistent with the EDS analysis.

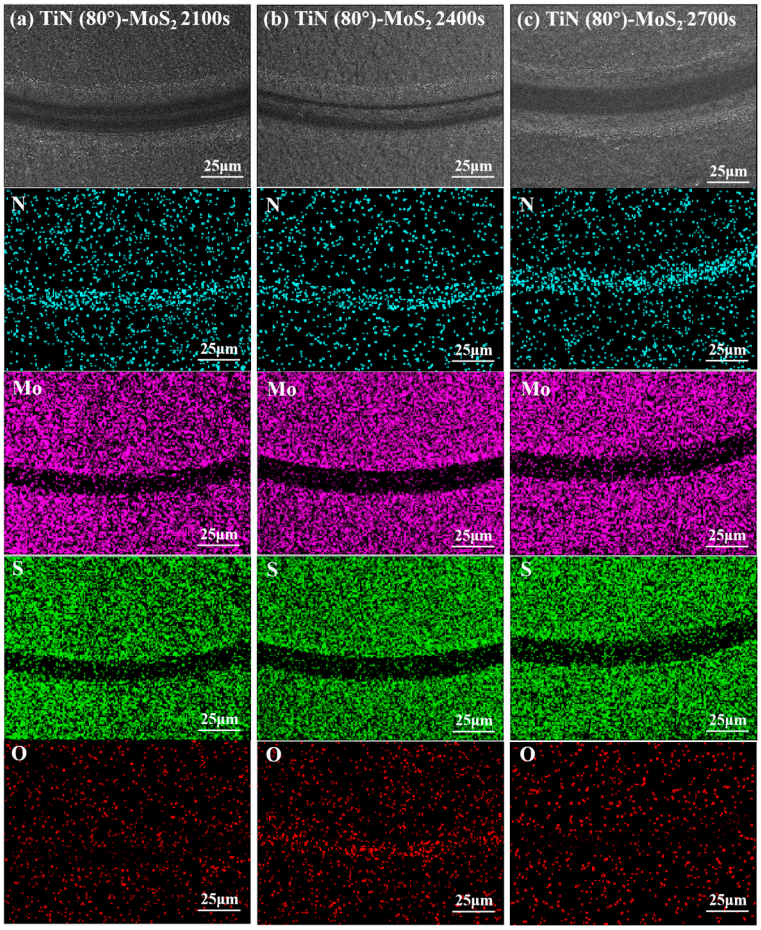

Figure 11. FESEM images and EDS mapping of the wear tracks of TiN–MoS_2 composite coatings during the humidity transition friction test: (**a**) TiN (80°)–MoS_2, 20% RH, 2100 s; (**b**) TiN (80°)–MoS_2, 70% RH, 2400 s; (**c**) TiN (80°)–MoS_2, 20% RH, 2700 s.

Based on these findings and analysis of the wear tracks, the tribological mechanism schematics of the TiN (80°)–MoS_2 composite coatings in humidity-fluctuating environments are given in Figure 14. At the initial stage of 20% RH, the MoS_2 on the coating surface acted as a lubricant and exhibited effective lubrication. As the humidity was alternated to 70% RH, the MoS_2 lubricant on the wear track of the coating was degraded owing to the oxidation and then removed by the fraction. At the same time, the fresh MoS_2 lubricant stored in the pores of the TiN columnar matrix could be released. The degradation of MoS_2 on the wear track and the release of fresh MoS_2 from the pores kept the COF was about 0.2 during this stage. After the environmental conditions shifted from 70% to 20% RH, the MoS_2 in TiN (80°)–MoS_2 composite coating could be released from the pores to play a lubricating role in a low-humid environment. In addition, all the oxidation products of the MoS_2 were removed, leading to a decrease in the COF. In contrast, TiN (0°)–MoS_2 cannot store MoS_2 due to its dense structure. During the humidity transition friction process, the MoS_2 lubricant on the surface was continuously consumed and removed, leading to a gradual increase in COF.

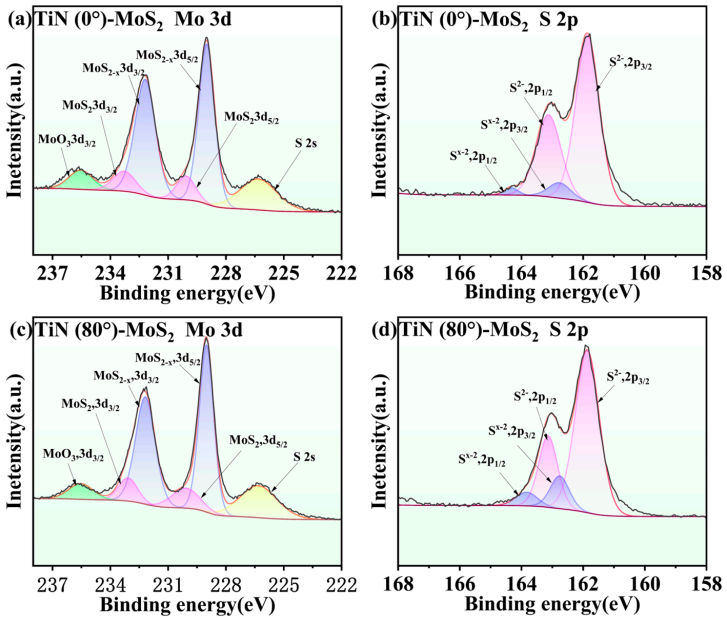

Figure 12. XPS spectra of the wear track from the TiN (0°)–MoS_2 and TiN (80°)–MoS_2 composite coatings during the sliding process of the humidity transition friction test at 70% RH at 2400 s.

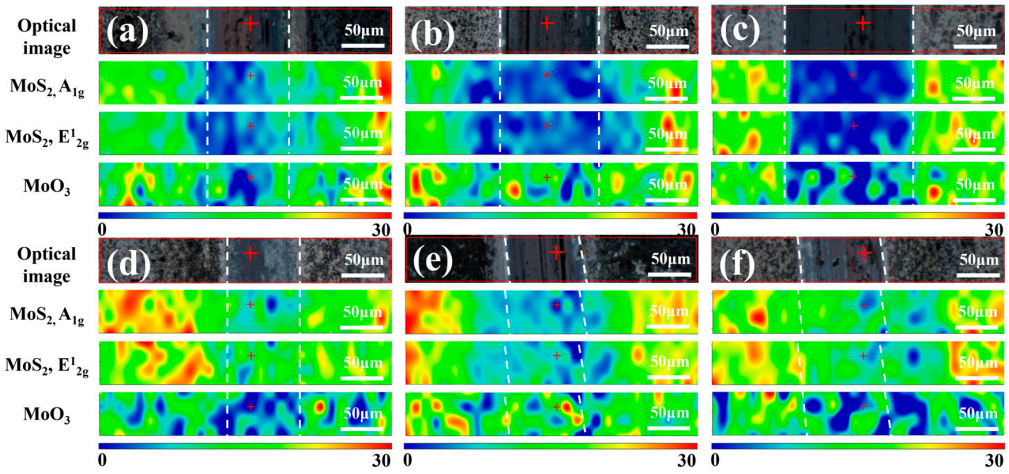

Figure 13. The optical images, MoS2 A1g and E12g peak intensity distribution mapping, and MoO3 peak intensity mapping of the wear track for (**a**–**c**) the TiN (0°)–MoS2 and (**d**–**f**) TiN (80°)–MoS2 composite coatings during the final three stages of the friction test in humidity-fluctuating environment.

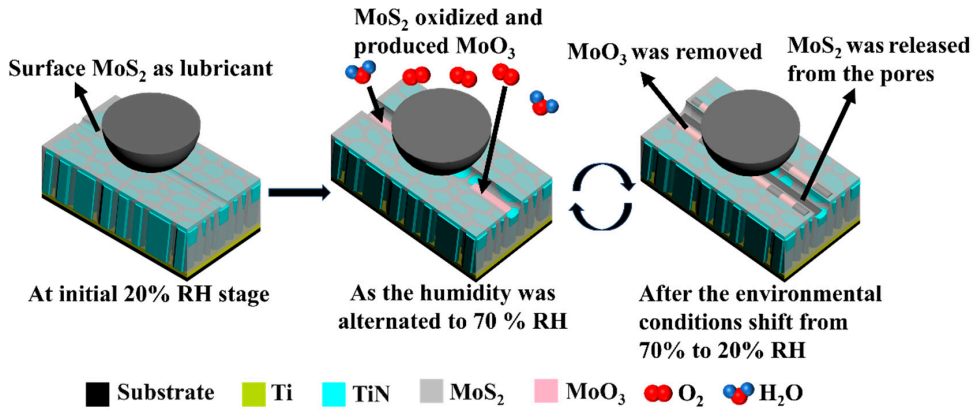

Figure 14. Schematic diagram of the self-lubricating mechanism of TiN (80°)–MoS_2 composite coating under humidity-fluctuation environments.

4. Conclusions

In this study, porous TiN coatings were prepared by DCMS technologies. Subsequently, MoS_2 was filled into the porous TiN coating through CVD to prepare the TiN–MoS_2 composite coating. The porous TiN coating not only stored a solid lubricant phase but also possessed a certain load-bearing capacity. The TiN (80°)–MoS_2 composite coating demonstrated an extended service life at 20% RH, 70% RH, and in a humidity-fluctuating environment. The results of the EDS, XPS, and Raman analyses of the wear tracks indicated that, at 20% RH, the MoS_2 stored in the pores of the TiN (80°)–MoS_2 composite coating was gradually released to the wear track surface, showing an excellent lubrication effect, and the COF was about 0.05. However, at 70% RH, MoS_2 reacted with H_2O and O_2 to produce MoO_3, which diminished the lubrication effect. At this stage, the COF was about 0.2, which was attributed to the degradation of the MoS_2 on the wear track and the release of fresh MoS_2 from the pores. After the environmental conditions shifted from 70 to 20% RH, all the oxides of the MoS_2 were removed, and the COF decreased. The TiN (80°)–MoS_2 composite coating exhibited excellent friction performance across various humidity environments, indicating its self-lubricating capabilities in these environments.

Compared with the previous research works mentioned in the introduction section, the porous TiN (80°)–MoS_2 composite coating presented a longer service life. However, the porous TiN (80°)–MoS_2 composite coating had a COF that resulted in it being higher than that of the TiCN–MoS_2 composite coating in the high humidity environment. Consequently, in future work, we will try to fill out the pores with another kind of solid lubricant in order to maintain the low COF of the coating in different environments.

Author Contributions: Conceptualization and methodology, K.L., Y.L. and L.Z.; formal analysis and investigation, K.L., G.W., Z.R., Y.L., L.Z. and S.X.; resources, L.Z. and H.T.; validation, T.Y.; writing—original draft, T.Y.; writing—review and editing, L.Z. and H.T. All authors have read and agreed to the published version of the manuscript.

Funding: This research was funded by the Strategic Priority Research Program of the Chinese Academy of Sciences (Grant No. XDB0470102), the fund of the Excellent Youth Science Foundation of Shandong Province (Grant No. 2022HWYQ-096), the fund of Natural Science Foundation of Shandong Province (Grant No. ZR2022QE162, ZR2024QA223, ZR2024QE526), the Key Research and Development Program in Shandong Province (No. SYS202203), the Key Research Project of Shandong Provincial Natural Science Foundation (No. ZR2023ZD13), the Scientific Instrument Development Program of the Chinese Academy of Sciences (No. PTYQ2024YZ0006), the Key Instrument Development Program of the National Natural Science Foundation of China (No. 52427807), the Key Research Project of Shandong Provincial Natural Science Foundation (No. 2024KJHZ017), and the Program for Taishan Scholars of Shandong Province.

Data Availability Statement: All the data mentioned in this paper.

Conflicts of Interest: The authors declare no conflict of interest.

References

1. Teer, D.G. New Solid Lubricant Coatings. *Wear* **2001**, *251*, 1068–1074. [CrossRef]
2. Wang, C.; Zhang, J.; Le, K.; Niu, Y.; Gao, X.; Che, Q.; Xu, S.; Liu, Y.; Liu, W. Effect of Substrate Roughness and Contact Scale on the Tribological Performance of MoS_2 Coatings. *Lubricants* **2023**, *11*, 191. [CrossRef]
3. Polcar, T.; Cavaleiro, A. Review on Self-Lubricant Transition Metal Dichalcogenide Nanocomposite Coatings Alloyed with Carbon. *Surf. Coat. Technol.* **2011**, *206*, 686–695. [CrossRef]
4. Liu, X.; Le, K.; Yang, W.; Liu, Y.; Luo, Y.; Zheng, X.; Chen, H.; Xu, S.; Liu, W. Tailoring the Crystallinity and Phase Composition of MoS_2 Nanosheets for Better Lubrication Performance. *Appl. Surf. Sci.* **2024**, *673*, 160856. [CrossRef]
5. Liu, X.; Le, K.; Wang, J.; Lin, H.; Liu, Y.; Jiang, F.; Yang, Z.; Li, H.; Xu, S.; Liu, W. Synergistic Lubrication of Multilayer $Ti_3C_2T_x$@MoS_2 Composite Coatings via Hydrothermal Synthesis. *Appl. Surf. Sci.* **2024**, *668*, 160400. [CrossRef]

6. Voevodin, A.A.; Fitz, T.A.; Hu, J.J.; Zabinski, J.S. Nanocomposite Tribological Coatings with "Chameleon" Surface Adaptation. *J. Vac. Sci. Technol. A Vac. Surf. Film.* **2002**, *20*, 1434–1444. [CrossRef]
7. Muratore, C.; Voevodin, A.A. Molybdenum Disulfide as a Lubricant and Catalyst in Adaptive Nanocomposite Coatings. *Surf. Coat. Technol.* **2006**, *201*, 4125–4130. [CrossRef]
8. Fan, X.; Shi, Y.; Cui, M.; Ren, S.; Wang, H.; Pu, J. MoS_2 /WS_2 Nanosheet-Based Composite Films Irradiated by Atomic Oxygen: Implications for Lubrication in Space. *ACS Appl. Nano Mater.* **2021**, *4*, 10307–10320. [CrossRef]
9. Ren, S.; Shang, K.; Cui, M.; Wang, L.; Pu, J.; Yi, P. Structural Design of MoS_2-Based Coatings toward High Humidity and Wide Temperature. *J. Mater. Sci.* **2019**, *54*, 11889–11902. [CrossRef]
10. Fleischauer, P.D.; Lince, J.R. A Comparison of Oxidation and Oxygen Substitution in MoS_2 Solid Film Lubricants. *Tribol. Int.* **1999**, *32*, 627–636. [CrossRef]
11. Chen, H.; Wang, W.; Le, K.; Liu, Y.; Gao, X.; Luo, Y.; Zhao, X.; Liu, X.; Xu, S.; Liu, W. Effects of Substrate Roughness on the Tribological Properties of Duplex Plasma Nitrided and MoS_2 Coated Ti6Al4V Alloy. *Tribol. Int.* **2024**, *191*, 109123. [CrossRef]
12. Rickerby, D.S.; Burnett, P.J. The Wear and Erosion Resistance of Hard PVD Coatings. *Surf. Coat. Technol.* **1987**, *33*, 191–211. [CrossRef]
13. Łępicka, M.; Grądzka-Dahlke, M.; Pieniak, D.; Pasierbiewicz, K.; Kryńska, K.; Niewczas, A. Tribological Performance of Titanium Nitride Coatings: A Comparative Study on TiN-Coated Stainless Steel and Titanium Alloy. *Wear* **2019**, *422–423*, 68–80. [CrossRef]
14. Borah, S.M.; Pal, A.R.; Bailung, H.; Chutia, J. Optimization of Plasma Parameters for High Rate Deposition of Titanium Nitride Films as Protective Coating on Bell-Metal by Reactive Sputtering in Cylindrical Magnetron Device. *Appl. Surf. Sci.* **2008**, *254*, 5760–5765. [CrossRef]
15. Yao, Y.; Wu, Y.; Zhang, Z.; Zhu, H.; Hu, M.; Xu, K.; Liu, Y. Enhancement of frictional properties of Ni-MoS_2 self-lubricating composite coatings by microgroove arrays. *Appl. Surf. Sci.* **2022**, *605*, 154635. [CrossRef]
16. Wang, Y.; Li, R.; Zhao, X.; Xue, Y.; An, Y.; Zhou, H.; Chen, J. The synergistic action of Ag and MoS_2 on tribological properties of Al_2O_3/Ag (MoS_2) composite coatings. *Surf. Coat. Technol.* **2023**, *466*, 129633. [CrossRef]
17. Gangopadhyay, S.; Acharya, R.; Chattopadhyay, A.K.; Paul, S. Effect of Substrate Bias Voltage on Structural and Mechanical Properties of Pulsed DC Magnetron Sputtered TiN–MoS_x Composite Coatings. *Vacuum* **2010**, *84*, 843–850. [CrossRef]
18. Goller, R.; Torri, P.; Baker, M.A.; Gilmore, R.; Gissler, W. The Deposition of Low-Friction TiN–MoS_x Hard Coatings by a Combined Arc Evaporation and Magnetron Sputter Process. *Surf. Coat. Technol.* **1999**, *120–121*, 453–457. [CrossRef]
19. Gilmore, R.; Baker, M.A.; Gibson, P.N.; Gissler, W.; Stoiber, M.; Losbichler, P.; Mitterer, C. Low-Friction TiN–MoS_2 Coatings Produced by Dc Magnetron Co-Deposition. *Surf. Coat. Technol.* **1998**, *108–109*, 345–351. [CrossRef]
20. Voevodin, A.A.; Zabinski, J.S. Laser Surface Texturing for Adaptive Solid Lubrication. *Wear* **2006**, *261*, 1285–1292. [CrossRef]
21. Basnyat, P.; Luster, B.; Muratore, C.; Voevodin, A.A.; Haasch, R.; Zakeri, R.; Kohli, P.; Aouadi, S.M. Surface Texturing for Adaptive Solid Lubrication. *Surf. Coat. Technol.* **2008**, *203*, 73–79. [CrossRef]
22. Liang, J.; Le, K.; Liu, Y.; Jang, Y.-J.; Jiang, F.; Yang, Z.; Li, H.; Xu, S.; Liu, W. Adaptive Tribological Performance of Porous TiCN-MoS_2 Composite Coatings in Response to Fluctuating Humidity Conditions. *Surf. Coat. Technol.* **2024**, *482*, 130666. [CrossRef]
23. Hawkeye, M.M.; Brett, M.J. Glancing Angle Deposition: Fabrication, Properties, and Applications of Micro- and Nanostructured Thin Films. *J. Vac. Sci. Technol. A* **2007**, *25*, 1317–1335. [CrossRef]
24. Barranco, A.; Borras, A.; Gonzalez-Elipe, A.R.; Palmero, A. Perspectives on Oblique Angle Deposition of Thin Films: From Fundamentals to Devices. *Prog. Mater. Sci.* **2016**, *76*, 59–153. [CrossRef]
25. Robbie, K.; Brett, M.J. Sculptured Thin Films and Glancing Angle Deposition: Growth Mechanics and Applications. *J. Vac. Sci. Technol. A* **1997**, *15*, 1460–1465. [CrossRef]
26. Xin, R.; Ruishan, Z.; Wei, W.; Xiaolong, S.; Yang, Z.; Chongyi, Z. Corrosion Resistance of TiCN Films Prepared with Combining Multi-Arc Ion Plating and Magnetron Sputtering Technique. *Rare Met. Mater. Eng.* **2018**, *47*, 2028–2036. [CrossRef]
27. Zhang, S.; Li, D.; Yoon, J.; Cho, T. Synthesis and Evaluation of TiN-WC/TiN Nanocomposite by the Hybrid Technique with Arc Ion Plating and Magnetron Sputtering. *Curr. Appl. Phys.* **2010**, *10*, 842–847. [CrossRef]
28. Coto, B.; Hallander, P.; Mendizabal, L.; Pagano, F.; Kling, H.; Ortiz, R.; Barriga, J.; Selegård, L. Particle and rain erosion mechanisms on Ti/TiN multilayer PVD coatings for carbon fibre reinforced polymer substrates protection. *Wear* **2021**, *466*, 203575. [CrossRef]
29. Yang, C.; Wang, R.; Jiang, B.; Hao, J. Effect of target power ratio on microstructure and deposition rate of TiN film deposited by dual pulse power magnetron sputtering. *Ceram. Int.* **2022**, *48*, 29652–29658. [CrossRef]
30. Wei, L.J.; Ma, D.L.; Xie, D.; Jing, P.P.; Leng, Y.X. The Performance and Stability of NiTi Photoactuator Utilizing Photothermal Effect of TiN Films with Tilted Columnar Structure. *Sens. Actuators A Phys.* **2024**, *368*, 115106. [CrossRef]
31. Phae-ngam, W.; Horprathum, M.; Chananonnawathorn, C.; Lertvanithphol, T.; Samransuksamer, B.; Songsiriritthigul, P.; Nakajima, H.; Chaiyakun, S. Oblique Angle Deposition of Nanocolumnar TiZrN Films via Reactive Magnetron Co-Sputtering Technique: The Influence of the Zr Target Powers. *Curr. Appl. Phys.* **2019**, *19*, 894–901. [CrossRef]

32. Verbeno, C.H.; Krohling, A.C.; Paschoa, A.; Bueno, T.E.P.; Soares, M.M.; Mori, T.J.A.; Larica, C.; Nascimento, V.P.; van Lierop, J.; Passamani, E.C. Cobalt Nanowire Arrays Grown on Vicinal Sapphire Templates by DC Magnetron Sputtering. *J. Magn. Magn. Mater.* **2020**, *507*, 166854. [CrossRef]
33. Dolatshahi-Pirouz, A.; Hovgaard, M.B.; Rechendorff, K.; Chevallier, J.; Foss, M.; Besenbacher, F. Scaling Behavior of the Surface Roughness of Platinum Films Grown by Oblique Angle Deposition. *Phys. Rev. B* **2008**, *77*, 115427. [CrossRef]
34. Vaz, F.; Machado, P.; Rebouta, L.; Mendes, J.A.; Lanceros-Méndez, S.; Cunha, L.; Nascimento, S.M.C.; Goudeau, P.; Rivière, J.P.; Alves, E.; et al. Physical and Morphological Characterization of Reactively Magnetron Sputtered TiN Films. *Thin Solid Film.* **2002**, *420–421*, 421–428. [CrossRef]
35. Luo, Q.; Yang, S.; Cooke, K.E. Hybrid HIPIMS and DC Magnetron Sputtering Deposition of TiN Coatings: Deposition Rate, Structure and Tribological Properties. *Surf. Coat. Technol.* **2013**, *236*, 13–21. [CrossRef]
36. Fox, V.C.; Renevier, N.; Teer, D.G.; Hampshire, J.; Rigato, V. The Structure of Tribologically Improved MoS_2-Metal Composite Coatings and Their Industrial Applications. *Surf. Coat. Technol.* **1999**, *116*, 492–497. [CrossRef]
37. Renevier, N.M.; Fox, V.C.; Teer, D.G.; Hampshire, J. Coating Characteristics and Tribological Properties of Sputter-Deposited MoS_2 Rmetal Composite Coatings Deposited by Closed Field Unbalanced Magnetron Sputter Ion Plating. *Surf. Coat. Technol.* **2000**, *127*, 24–37. [CrossRef]
38. Sun, G.; Du, L.; Hu, J.; Zhang, B.; Misra, R.D. On the influence of deformation mechanism during cold and warm rolling on annealing behavior of a 304 stainless steel. *Mat. Sci. Eng. A Struct.* **2019**, *746*, 341–355. [CrossRef]
39. Qin, X.; Ke, P.; Wang, A.; Kim, K.H. Microstructure, Mechanical and Tribological Behaviors of MoS_2-Ti Composite Coatings Deposited by a Hybrid HIPIMS Method. *Surf. Coat. Technol.* **2013**, *228*, 275–281. [CrossRef]
40. Dupin, J.C.; Gonbeau, D.; Martin-Litas, I.; Vinatier, P.; Levasseur, A. Amorphous Oxysulfide thin films MO_yS_z (M = W, Mo, Ti) XPS Characterization: Structural and Electronic Pecularities. *Appl. Surf. Sci.* **2001**, *173*, 140–150. [CrossRef]
41. Bai, Y.; Pu, J.; Wang, H.; Wang, L.; Xue, Q.; Liu, S. High Humidity and High Vacuum Environment Performance of MoS_2/Sn Composite Film. *J. Alloys Compd.* **2019**, *800*, 107–115. [CrossRef]
42. Windom, B.C.; Sawyer, W.G.; Hahn, D.W. A Raman Spectroscopic Study of MoS_2 and MoO_3: Applications to Tribological Systems. *Tribol. Lett.* **2011**, *42*, 301–310. [CrossRef]
43. Santos, E.B.; de Souza e Silva, J.M.; Mazali, I.O. Raman Spectroscopy as a Tool for the Elucidation of Nanoparticles with Core–Shell Structure of TiO_2 and MoO_3. *Vib. Spectrosc.* **2010**, *54*, 89–92. [CrossRef]